Title

The TESS-Keck Survey. XXII. A Sub-Neptune Orbiting TOI-1437

Journal

The Astronomical Journal, 168(3)

ISSN

0004-6256

Authors

Pidhorodetska, Daria
Gilbert, Emily A
Kane, Stephen R
et al.

Publication Date

2024-09-01

DOI

10.3847/1538-3881/ad6901

The Astronomical Journal, 168:135 (9pp), 2024 September https://doi.org/10.3847/1538-3881/ad6901

The TESS-Keck Survey. XXII. A Sub-Neptune Orbiting TOI-1437

Daria Pidhorodetska[1,27], Emily A. Gilbert[2], Stephen R. Kane[1], Thomas Barclay[3], Alex S. Polanski[4], Michelle L. Hill[1,27], Keivan G. Stassun[5], Steven Giacalone[6,28], David R. Ciardi[7], Andrew W. Boyle[6], Steve B. Howell[8], Jorge Lillo-Box[9], Mason G. MacDougall[10], Tara Fetherolf[1,11], Natalie M. Batalha[12], Ian J. M. Crossfield[4], Courtney Dressing[13], Benjamin Fulton[14], Andrew W. Howard[15], Daniel Huber[16,17], Howard Isaacson[18,19], Erik A. Petigura[10], Paul Robertson[20], Lauren M. Weiss[21], Isabel Angelo[10], Corey Beard[20], Aida Behmard[22,29], Sarah Blunt[23], Casey L. Brinkman[16], Ashley Chontos[24], Fei Dai[6,16,25], Paul A. Dalba[12], Rae Holcomb[20], Jack Lubin[10,20], Andrew W. Mayo[13], Joseph M. Akana Murphy[12,30], Malena Rice[26], Ryan Rubenzahl[6], Nicholas Scarsdale[12], Emma V. Turtelboom[13], Dakotah Tyler[10], Judah Van Zandt[10], and Edward W. Schwieterman[1]

[1] Department of Earth and Planetary Sciences, University of California, Riverside, CA 92521, USA
[2] Jet Propulsion Laboratory, California Institute of Technology, 4800 Oak Grove Drive, Pasadena, CA 91109, USA
[3] NASA Goddard Space Flight Center, 8800 Greenbelt Road, Greenbelt, MD 20771, USA
[4] Department of Physics and Astronomy, University of Kansas, Lawrence, KS 66045, USA
[5] Department of Physics and Astronomy, Vanderbilt University, Nashville, TN 37235, USA
[6] Department of Astronomy, California Institute of Technology, Pasadena, CA 91125, USA
[7] NASA Exoplanet Science Institute—Caltech/IPAC, Pasadena, CA 91125, USA
[8] NASA Ames Research Center, Moffett Field, CA 94035, USA
[9] Centro de Astrobiología (CAB), CSIC-INTA, ESAC campus, Camino Bajo del Castillo s/n, 28692, Villanueva de la Cañada (Madrid), Spain
[10] Department of Physics & Astronomy, University of California Los Angeles, Los Angeles, CA 90095, USA
[11] Department of Physics, California State University, San Marcos, CA 92096, USA
[12] Department of Astronomy and Astrophysics, University of California, Santa Cruz, CA 95060, USA
[13] Department of Astronomy, University of California Berkeley, Berkeley, CA 94720, USA
[14] NASA Exoplanet Science Institute/Caltech-IPAC, MC 314-6, 1200 E California Boulevard, Pasadena, CA 91125, USA
[15] California Institute of Technology, Pasadena, CA 91125, USA
[16] Institute for Astronomy, University of Hawai'i, 2680 Woodlawn Drive, Honolulu, HI 96822, USA
[17] Sydney Institute for Astronomy (SIfA), School of Physics, University of Sydney, NSW 2006, Australia
[18] Department of Astronomy, University of California, Berkeley, Berkeley, CA 94720, USA
[19] Centre for Astrophysics, University of Southern Queensland, Toowoomba, QLD, Australia
[20] Department of Physics and Astronomy, University of California, Irvine, CA 92697, USA
[21] Department of Physics and Astronomy, University of Notre Dame, Notre Dame, IN 46556, USA
[22] Department of Astrophysics, American Museum of Natural History, 200 Central Park West, Manhattan, NY 10024, USA
[23] Center for Interdisciplinary Exploration and Research in Astrophysics (CIERA), Northwestern University, Evanston, IL 60208, USA
[24] Department of Astrophysical Sciences, Princeton University, Princeton, NJ, 08544, USA
[25] Division of Geological and Planetary Sciences, 1200 E California Boulevard, Pasadena, CA, 91125, USA
[26] Department of Astronomy, Yale University, New Haven, CT 06511, USA
Received 2024 March 19; revised 2024 July 15; accepted 2024 July 23; published 2024 August 30

Abstract

Exoplanet discoveries have revealed a dramatic diversity of planet sizes across a vast array of orbital architectures. Sub-Neptunes are of particular interest; due to their absence in our own solar system, we rely on demographics of exoplanets to better understand their bulk composition and formation scenarios. Here, we present the discovery and characterization of TOI-1437 b, a sub-Neptune with a 18.84 day orbit around a near-solar analog ($M_\star = 1.10 \pm 0.10\,M_\odot$, $R_\star = 1.17 \pm 0.12\,R_\odot$). The planet was detected using photometric data from the Transiting Exoplanet Survey Satellite (TESS) mission and radial velocity (RV) follow-up observations were carried out as a part of the TESS-Keck Survey using both the HIRES instrument at Keck Observatory and the Levy Spectrograph on the Automated Planet Finder telescope. A combined analysis of these data reveal a planet radius of $R_p = 2.24 \pm 0.23\,R_\oplus$ and a mass measurement of $M_p = 9.6 \pm 3.9\,M_\oplus$). TOI-1437 b is one of few (~50) known transiting sub-Neptunes orbiting a solar-mass star that has a RV mass measurement. As the formation pathway of these worlds remains an unanswered question, the precise mass characterization of TOI-1437 b may provide further insight into this class of planet.

Unified Astronomy Thesaurus concepts: Exoplanets (498); Radial velocity (1332); Mini Neptunes (1063)

Materials only available in the online version of record: machine-readable table

[27] NASA FINESST Fellow.
[28] NSF Astronomy and Astrophysics Postdoctoral Fellow.
[29] Kalbfleisch Fellow.
[30] NSF Graduate Research Fellow.

1. Introduction

In the ever-expanding field of exoplanetary research, each discovery marks a stride toward unraveling the mysteries of distant worlds. The CoRoT (Léger et al. 2009), Kepler (Borucki et al. 2010), and K2 missions (Howell et al. 2014) paved the way for space-based detection of planets smaller than Neptune ($\lesssim 4R_\oplus$) through the use of the transit method. Although Kepler identified a plethora of sub-Neptunes within our Galaxy (Dressing & Charbonneau 2013; Fulton et al. 2018), relatively few of these planets were suitable radial velocity (RV) follow-up targets as a result of their large distances.

The formation (e.g., Rogers et al. 2011; Schlichting 2014; Raymond et al. 2018), atmospheric composition (e.g., Morley et al. 2017; Kempton et al. 2018), and interior structure (e.g., Guzmán-Mesa et al. 2022; Misener et al. 2023) of sub-Neptunes are not well understood. These planets, ranging from 1 to 4 $R_\oplus$, are expected to vary in composition from rocky to gas-rich (Fortney et al. 2013; Moses et al. 2013; Lopez & Fortney 2014), while planets with radii larger than 1.6 $R_\oplus$ retain hydrogen envelopes (Rogers 2015; Fulton et al. 2017). The mass–radius relation can provide the initial assessment of how likely it is that the planet hosts an atmosphere, but these parameters are often unknown. Although around a third of Sun-like stars host sub-Neptunes with orbital periods of less than 100 days (Fressin et al. 2013; Petigura et al. 2013; Burke et al. 2015; Hsu et al. 2019), relatively few (∼50) of these planets have known mass measurements. This strengthens the need for RV observations of these worlds to further understand their nature.

The Transiting Exoplanet Survey Satellite (TESS; Ricker et al. 2015) has added to the exoplanet inventory by carrying out an all-sky survey attempting to detect small, transiting planets around bright, nearby stars. Revealing over 6000 planet candidates thus far, many of these TESS Objects of Interest are amenable to follow-up with RV measurements to determine planetary masses (Guerrero et al. 2021; Kane et al. 2021b). The TESS-Keck Survey (Chontos et al. 2022), a large monitoring program of TESS planet candidates with the Keck-HIRES and APF-Levy Spectrographs, is working to provide the precise planet mass measurements required by future efforts targeting atmospheric characterization that often include sub-Neptunes (e.g., Scarsdale et al. 2021; Lubin et al. 2022; Lange 2024). Measurements of planet radii in combination with masses have proven to be the most advantageous method for understanding the compositions of exoplanets by allowing us to discern the bulk densities of planets (Howe et al. 2014; Lopez & Fortney 2014; Wolfgang et al. 2016; Unterborn et al. 2023). These combined measurements are particularly important for sub-Neptune exoplanets that have no analog representation within the solar system (Kane et al. 2021a).

Here, we announce the discovery and precise mass measurement of a planet orbiting TOI-1437 (otherwise known as HD 154840; BD+57 1730; TIC 198356533), a near-solar analog ($M_\star$=1.10 ± 0.10 $M_\odot$, $R_\star$=1.17 ± 0.12 $R_\odot$) observed by TESS. Section 2 describes the observations and collected data of the system including photometry, spectroscopy, and imaging. Section 3 details the host star properties, followed by an analysis of the data modeling in Section 4. A discussion of the results and findings is found in Section 5 with concluding remarks in Section 6.

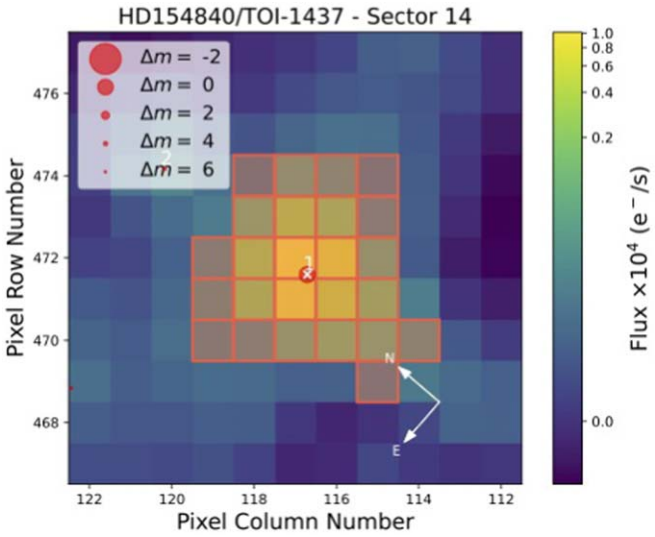

Figure 1. Target pixel file corresponding to TOI-1437 observations by TESS in Sector 14. Sources from Gaia DR3 are shown as red circles, with their size corresponding to the magnitude contrast against TOI-1437 (marked with the label "1" and a white cross). The aperture used by the TESS-SPOC pipeline is shown as a shaded red region in each panel.

2. Observations

2.1. Photometry

TOI-1437 lies within the northern Continuous Viewing Zone, which has been observed exhaustively by TESS over its full mission lifetime. TESS observed TOI-1437 in year 2 of operations at a 2 minute cadence during Sectors 14–26. TOI-1437 was also observed in Sectors 40, 41, and 47–60, at both 20 s and 2 minute cadences. TOI-1437 will be reobserved by TESS in upcoming Sectors 73–83. The time-series observations of TOI-1437 were processed with the TESS Science Processing Operations Center (SPOC) pipeline (Jenkins et al. 2016), which resulted in the detection of a periodic transit signal for TOI-1437.01 that was alerted on 2019 November 14. No significant photometric variability is present in the light curve data.

To check for sources of contamination within the pipeline aperture, we use the `tpfplotter` algorithm[31] to inspect the target pixel files (TPFs) for each sector using the procedure described in Aller et al. (2020). Figure 1 shows the TPF of Sector 14 overlaid with the Gaia Data Release 3 (DR3) catalog (Gaia Collaboration et al. 2023) consisting of bright sources down to 6 mag more faint than TOI-1437. The TPF shows no indication of any sources of contamination within the aperture of TESS.

2.2. Spectroscopy

2.2.1. HIRES Observations

TOI-1437 was observed over 88 nights with the HIRES instrument at the Keck Observatory (Vogt et al. 1994) between UT 2019 November 28 and UT 2023 June 26, including one high signal-noise-ratio iodine-free template spectrum. HIRES is an echelle spectrometer which observes over a spectral range of 3000–6500 Å. HIRES uses the iodine technique, where the wavelength range for RV measurements is 5000–6300 Å. As

[31] https://github.com/jlillo/tpfplotter

Table 1
Radial Velocity Measurements

Time (BJD)	RV (m s^{-1})	RV Unc. (m s^{-1})	S_{HK}	Instrument
2458831.077696	−2.23	5.72	0.1450	Levy
2458831.091608	7.68	6.27	0.1375	Levy
2458852.10649	21.07	6.69	0.1171	Levy
2458876.070009	−12.17	7.14	0.1286	Levy
2458876.084558	−1.64	7.14	0.1337	Levy
2458882.049758	−4.89	10.49	0.1440	Levy
2458883.941799	14.17	12.18	0.0974	Levy
2458885.042157	−0.77	10.22	0.3082	Levy
2458885.87575	24.68	10.37	0.1557	Levy
2458887.016514	1.33	6.57	0.1255	Levy
2458917.092394	0.54	1.90	0.1204	HIRES
2458918.07703	3.10	1.73	0.126	HIRES
2458999.90562	−0.34	1.62	0.1301	HIRES
2459002.948851	1.34	1.57	0.1289	HIRES
2459003.911424	0.81	1.55	0.1304	HIRES
2459006.907673	1.43	1.36	0.1308	HIRES
2459007.899261	1.39	1.36	0.1301	HIRES
2459010.936502	−1.20	1.43	0.1305	HIRES
2459011.850521	0.09	1.37	0.1316	HIRES
2459012.801402	4.34	1.49	0.1335	HIRES

Note. Only the first 10 APF/Levy and Keck/HIRES RVs are displayed in this table. A complete list has been made available online. S_{HK} values were measured using procedures from Isaacson & Fischer (2010) with standard uncertainties of 0.002 for APF/Levy measurements and 0.001 for Keck/HIRES measurements.

(This table is available in its entirety in machine-readable form in the online article.)

there are no prominent telluric lines in the wavelength section used in the iodine-cell technique, they are not masked out. For microtellurics (small absorption features caused by the atmosphere) or lines such as the Sodium D lines that can be in emission due to street light reflection in the atmosphere, the iodine technique implements a weighting technique that gives higher weights to the spectral segments that provide less scatter through an observation stack for each star. This effectively de-weights wavelength sections with problematic telluric features. Our HIRES RVs have a median binned uncertainty of 1.49 m s^{-1} and a median exposure time of 329 s. We reduced the RVs using the standard procedure described in Howard et al. (2010). The first ten HIRES RV measurements are provided in Table 1 while a complete list is available online.

2.2.2. APF Observations

In addition to the Keck/HIRES observations, we collected 106 spectra of TOI-1437 with the Levy Spectrograph on the Automated Planet Finder (APF) telescope (Vogt et al. 2014) between UT 2019 December 13 and 2022 July 30. The APF is a 2.4 m telescope located at the Mt. Hamilton station of UCO/Lick Observatory. The telescope is coupled with the high-resolution ($R_{max} \sim 120{,}000$) prism cross-dispersed Levy echelle spectrograph, which covers a wavelength range of ∼3700–9700 Å. APF uses the same iodine technique as HIRES, taking RV measurements between 5000 and 6300 Å and negating the need to mask out telluric lines. Our APF RVs have a median binned uncertainty of 5.22 m s^{-1} and a median exposure time of 1800 s. The APF/Levy Doppler software was developed based on the Keck/HIRES Doppler software and therefore follows a similar process for reducing spectra to RVs. A full description of the design and individual components of the APF is available in Vogt et al. 2014. The first ten APF RV measurements are provided in Table 1.

2.3. Imaging

Close stellar companions (bound or line of sight) can confound exoplanet discoveries in a number of ways. The detected transit signal might be a false positive due to a background eclipsing binary, and even real planet discoveries will yield incorrect stellar and exoplanet parameters if a close companion exists and are unaccounted for (Ciardi et al. 2015; Furlan & Howell 2020). Additionally, the presence of a close companion star leads to the non-detection of small planets residing with the same exoplanetary system (Lester et al. 2021). Given that nearly one-half of solar-like stars are in binary or multiple star systems (Matson et al. 2018), high-resolution imaging provides crucial information toward our understanding of exoplanetary formation, dynamics and evolution (Howell et al. 2021).

As part of our standard process for validating transiting exoplanets to assess the the possible contamination of bound or unbound companions on the derived planetary radii (Ciardi et al. 2015), we observed TOI-1437 with high-resolution near-infrared adaptive optics (AO) imaging at Palomar and Lick Observatories and in the optical with lucky imaging at Calar Alto and speckle imaging at Gemini North. The infrared observations provide the deepest sensitivities to faint companions, while the optical speckle observations provide the highest resolution imaging, making the two techniques complementary.

2.3.1. Palomar AO

The Palomar Observatory observations were made with the PHARO instrument (Hayward et al. 2001) behind the natural guide star AO system P3K (Dekany et al. 2013) on UT 2021 June 22 in a standard 5-point quincunx dither pattern with steps of 5″ in the narrow-band $Br-\gamma$ filter ($\lambda_o = 2.1686$; $\Delta\lambda = 0.0326$ μm). Each dither position was observed three times, offset in position from each other by 0.″5 for a total of 15 frames; with an integration time of 1.4 s per frame, the total on-source time was 21 s. PHARO has a pixel scale of 0.″025 per pixel for a total field of view of ∼25″. The science frames were flat-fielded and sky-subtracted. The reduced science frames were combined into a single image with a final resolution of 0.″091 FWHM (Figure 2).

To within the limits of the AO observations, no stellar companions were detected. The sensitivities of the final combined AO image were determined by injecting simulated sources azimuthally around the primary target every 20° at separations of integer multiples of the central source's FWHM (Furlan et al. 2017; Lund & Ciardi 2020). The brightness of each injected source was scaled until standard aperture photometry detected it with 5σ significance. The resulting brightness of the injected sources relative to TOI-1437 set the contrast limits at that injection location. The final 5σ limit at each separation was determined from the average of all of the determined limits at that separation, and the uncertainty on the limit was set by the rms dispersion of the azimuthal slices at a given radial distance.

2.3.2. Shane AO

We observed TOI-1437 on UT 2021 March 05 using the ShARCS camera on the Shane 3 m telescope at Lick

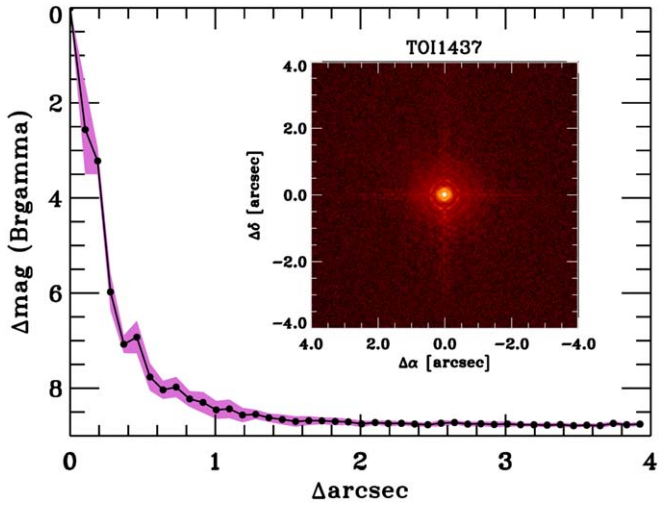

Figure 2. Companion sensitivity for the near-infrared adaptive optics imaging. The black points represent the 5σ limits and are separated in steps of 1 FWHM; the purple represents the azimuthal dispersion (1σ) of the contrast determinations. The inset image is of the primary target showing no additional close-in companions.

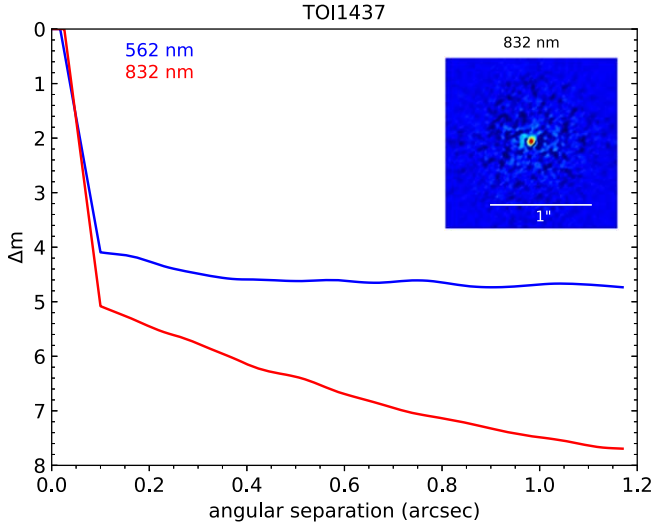

Figure 3. Companion sensitivity for speckle imaging. Contrast curves (5σ) for 562 nm are shown in blue and 832 nm in red. The reconstructed 832 nm speckle image (top right) shows that no close companions to TOI-1437 were detected within the obtained contrast and angular limits.

Observatory (Kupke et al. 2012; Gavel et al. 2014; McGurk et al. 2014). Observations were taken with the Shane AO system in natural guide star mode in order to search for nearby, unresolved stellar companions. We collected sequences of observations using a K_s filter ($\lambda_0 = 2.150\ \mu$m, $\Delta\lambda = 0.320\ \mu$m) and a J filter ($\lambda_0 = 1.238\ \mu$m, $\Delta\lambda = 0.271\ \mu$m). We reduced the data using the publicly available `SImMER` pipeline (Savel et al. 2020, 2022).[32] Our observations achieve contrasts of 4.5 (K_s) and 4.0 (J) at 1″. We find no nearby stellar companions within our detection limits.

2.3.3. Gemini Speckle

TOI-1437 was observed on UT 2020 February 18 using the 'Alopeke speckle instrument on the Gemini North 8 m telescope (Scott et al. 2021). 'Alopeke provides simultaneous speckle imaging in two bands (562 nm and 832 nm) with output data products including a reconstructed image with robust contrast limits on companion detections (Howell & Furlan 2022). Three sets of 1000×0.06 s images were obtained and processed in our standard reduction pipeline (see Howell et al. 2011). We find that TOI-1437 is a single star with no close companions brighter then 5–7.5 mag below that of the target star and within the angular and contrast limits achieved (Figure 3). The angular limits, the Gemini 8 m telescope diffraction limit (20 mas) out to 1.″2, correspond to spatial limits of 2–124 au at the distance of TOI-1437 ($d = 103$ pc). The 562 and 832 nm bands allow us to rule out close companions brighter than an M2V or an M4V, respectively.

2.3.4. Calar Alto Lucky

We obtained a high-spatial-resolution image of TOI-1437 using the AstraLux instrument (Hormuth et al. 2008), located at the 2.2 m telescope of the Calar Alto Observatory (Almería, Spain). The observations were executed on the night of UT 2020 February 25 under moderately poor weather conditions (average seeing of 1.″5) and at an airmass of 1.08. We obtained 54,457 frames in the SDSSz bandpass with an individual exposure time of 10 ms and a field of view windowed to $6'' \times 6''$. The datacube was then processed by the automatic observatory pipeline (Hormuth et al. 2008), which besides doing the basic reduction of the individual frames, selects the 10% with the highest Strehl ratio (Strehl 1902) and combines them into a final high-spatial-resolution image. This final image does not show any additional companions within the sensitivity limits. Such limits are computed using our own developed `astrasens` package[33] with the procedure described in Lillo-Box et al. (2012, 2014).

Subsequently, we used this contrast curve to establish the probability that the observed signal came from a chance-aligned eclipsing binary with capabilities of producing a transit depth mimicking the one observed and that could have been missed by our high-spatial-resolution image. We call this probability the blended source confidence (BSC) and the steps for estimating it are fully described in Lillo-Box et al. (2014). We use a Python implementation of this approach (`bsc` by J. Lillo-Box), which uses the TRILEGAL[34] galactic model (v1.6; Girardi et al. 2012) to retrieve a simulated source population of the region around the corresponding target.[35] We used the same parameters as in previous works (e.g., Bluhm et al. 2021; Soto et al. 2021), namely the default parameters for the bulge, halo, thin/thick disks, and the lognormal initial mass function from Chabrier (2001). The results from the BSC analysis are shown in Figure 4 and show a very low probability of 0.076% for our target to have a blended, undetected, eclipsing binary capable of mimicking our transit. Consequently, we assume from here on that the transit is associated with TOI-1437 and that it is not caused by any other source.

[32] https://github.com/arjunsavel/SImMER

[33] https://github.com/jlillo/astrasens

[34] http://stev.oapd.inaf.it/cgi-bin/trilegal

[35] This is done in python by using the `astrobase` implementation by Bhatti et al. (2020).

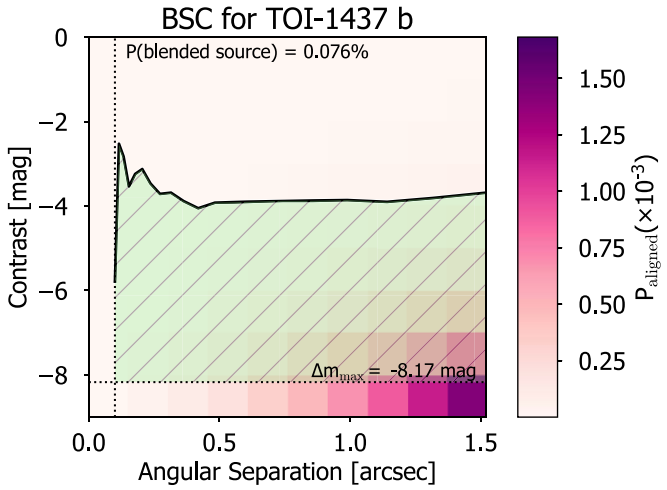

Figure 4. Results of the blended source confidence (BSC) analysis of Calar Alto Lucky imaging data indicate that the probability for TOI-1437 to have a blended, undetected, eclipsing binary capable of mimicking our transit is very low (0.076%).

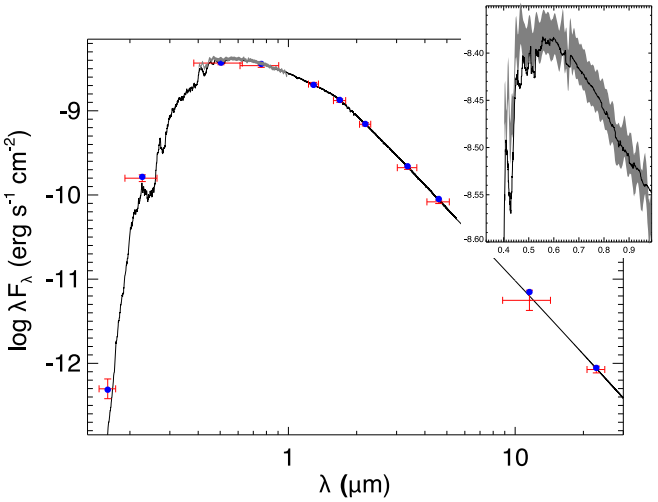

Figure 5. Spectral energy distribution of TOI-1437. Red symbols represent the observed photometric measurements, where the horizontal bars represent the effective width of the passband. Blue symbols are the model fluxes from the best-fit PHOENIX atmosphere model (black). The inset shows the absolute flux-calibrated Gaia spectrum as a gray swathe overlaid on the model.

3. Stellar Characterization

3.1. Gaia Assessment

In addition to the high-resolution imaging, we have utilized Gaia to identify any wide stellar companions that may be bound members of the system. Typically, these stars are already in the TESS Input Catalog and their flux dilution to the transit has already been accounted for in the transit fits and associated derived parameters. Based upon similar parallaxes and proper motions (e.g., Mugrauer & Michel 2020, 2021; Mugrauer et al. 2022), there are no additional widely separated companions identified by Gaia.

Additionally, the Gaia DR3 astrometry provides information on the possibility of inner companions that may have gone undetected by either Gaia or the high-resolution imaging. The Gaia Renormalised Unit Weight Error (RUWE) is a metric, similar to a reduced chi-square, where values that are $\lesssim$1.4 indicate that the Gaia astrometric solution is consistent with the star being single whereas RUWE values $\gtrsim$1.4 may indicate an astrometric excess noise, possibly caused the presence of an unseen companion (e.g., Ziegler et al. 2020). TOI-1437 has a Gaia DR3 RUWE value of 0.996 indicating that the astrometric fits are consistent with the single star model.

3.2. Stellar Properties

As an independent determination of the basic stellar parameters, we performed an analysis of the broadband spectral energy distribution (SED) of the star together with the Gaia DR3 parallax (with no systematic offset applied; see, e.g., Stassun & Torres 2021), in order to determine an empirical measurement of the stellar radius, following the procedures described in Stassun & Torres (2016) and Stassun et al. (2017, 2018). We pulled the JHK_S magnitudes from 2MASS, the W1–W4 magnitudes from WISE, the $G_{BP}G_{RP}$ magnitudes from Gaia DR3, and the FUV and NUV magnitudes from GALEX. We adopted a minimum uncertainty of 0.03 mag to account for known systematics in the absolute flux calibration of the ground-based photometric systems (see, e.g., Stassun & Torres 2016). We also utilized the absolute flux-calibrated low-resolution Gaia spectra. Together, the available photometry spans the full stellar SED over the wavelength range 0.2–20 μm (see Figure 5).

We performed a fit using PHOENIX stellar atmosphere models (Husser et al. 2013), with the principal parameters being the effective temperature ($T_{\rm eff}$) and metallicity ([Fe/H]), for which we adopted the spectroscopically determined values, as well as the extinction A_V, which we limited to the maximum line-of-sight value from the Galactic dust maps of Schlegel et al. (1998). The resulting model (Figure 5) has a best-fit $A_V = 0.04 \pm 0.02$ with a reduced χ^2 of 0.8.

Integrating the (unreddened) model SED gives the bolometric flux at Earth, $F_{\rm bol}$, which with the Gaia parallax directly yields the bolometric luminosity, $L_{\rm bol}$. Taking the $L_{\rm bol}$ and $T_{\rm eff}$ together provides us with the stellar radius, $R_\star$. This radius, along with the determined log g, allows us to derive a stellar mass that is consistent with the Torres et al. (2010) relations. A full list of the characterized stellar parameters is presented in Table 2.

Table 2
TOI-1437 Stellar Properties

Parameter	Value	Notes
R.A. (°)	256.1387540990	A
Decl. (°)	56.8425461418	A
μ_α (mas yr^{-1})	10.799 ± 0.013	A
$\mu\delta$ (mas yr^{-1})	-20.284 ± 0.015	A
ϖ (mas)	9.667 ± 0.010	A
[Fe/H]	-0.4924 ± -0.4983	A
V (mag)	9.173 ± 0.003	B
B (mag)	9.749 ± 0.042	B
$E_{(B-V)}$	0.0059 ± 0.0027	B
$T_{\rm eff}$ (K)	6008 ± 113	C
Luminosity ($L_\odot$)	1.926 ± 0.023	C
$F_{\rm bol}$ (erg s^{-1} cm^{-2})	$5.774 \pm 0.068 \times 10^{-9}$	C
log g	4.26 ± 0.04	C
Mass ($M_\odot$)	1.10 ± 0.10	C
ρ_* (g cc^{-1})	0.5023904	C

Note. A: Gaia DR3 (Gaia Collaboration et al. 2023); B: TIC v8.2; C: SED analysis

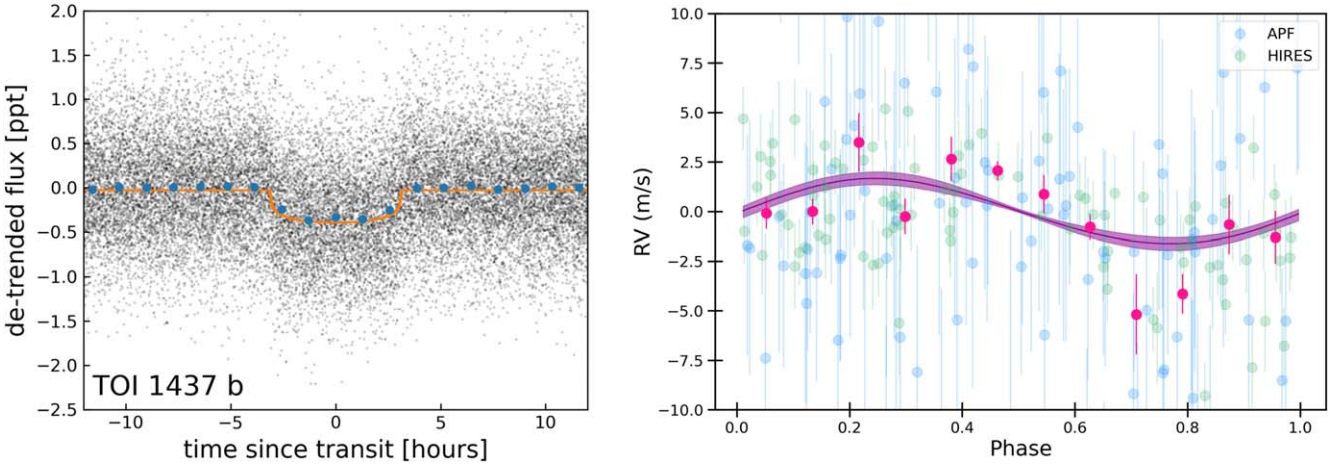

Figure 6. Left: transit model drawn from parameter posterior distributions fit from phase-folded TESS photometry of TOI-1437. The gray dots show the TESS 2 minutes cadence data. The orange line shows the best fit to each individual transit using `exoplanet`. The blue dots show the data binned to 2 minutes cadence. Right: phase-folded views of the best-fit RV model for TOI-1437 b (purple). Data from APF is shown in blue while HIRES is displayed in green, and each is binned to 12 total bins.

Table 3
Modeled Parameters and Priors

Parameter	Value/Source
Stellar Radius ($R_\odot$)	N(1.1765, 0.114)
Stellar Density ($\rho_\odot$)	LN(ln(0.99), 0.25)
Orbital Period (days)	N(18.841,0.001)
Transit Epoch (BJD)	N(2459906.55,0.02)
Planet-to-star Radius Ratio	LN(ln(0.0003), 2)
Impact Parameter	U(0,1+($r/R_\star$))
Limb Darkening u_1	Kipping (2013a)
Limb Darkening u_2	Kipping (2013a)
Orbital Eccentricity	UnitDisk/Kipping (2013b)
Periastron Angle (rad)	UnitDisk
RV Semiamplitude (m s^{-1})	LN(ln(2), 5)
TESS Jitter (ppt)	InverseGamma(93,41)
TESS Zero-point (ppt)	N(0,1)
TESS GP ρ (days)	InverseGamma(3.3,5.3)
TESS GP σ (ppt)	InverseGamma(93,41)
HIRES Jitter (m s^{-1})	InverseGamma(1.5,0.6)
HIRES Zero-point (m s^{-1})	N(0,3)
APF Jitter (m s^{-1})	InverseGamma(0.8,0.04)
APF Zero-point (m s^{-1})	N(0,3)
RV GP ρ (days)	InverseGamma(3,40)
RV GP σ (m s^{-1})	InverseGamma(0.8,0.04)

4. Analysis

4.1. Photometric and RV Analysis

A joint model for the TESS light curve data and the two RV data sets from HIRES and APF (Figure 6) was constructed using the framework provided by the `exoplanet` package (Foreman-Mackey et al. 2021). All available 2 minute cadence data (Section 2.1) was used. For this analysis, we did not include the 20 s cadence data. We normalized each sector to the median flux, centered on zero and combined the data into a single time series where the baseline was removed. We then sigma clipped the data for outliers more than 7σ from the data median. All but one of the 20 clipped points were positive outliers. We also put these data on a time axis centered on zero (e.g., the center of the data set) as this can reduce correlations between orbital period and transit epoch. For the RV data, the two instruments were treated as independent data sets. Each set was centered on median zero (m s^{-1}) and placed on the same time coordinates as the light curve data.

The model used Gaussian processes (GPs) to account for correlated noise in both the RV data and the light curve, and the GP hyperparameters are the same for the two RV data sets. The GP used is a nonperiodic simple harmonic oscillator implemented using the celerite2 software (Foreman-Mackey et al. 2017; Foreman-Mackey 2018). To avoid overfitting, we also modeled the RV data without the use of a GP and determined that a non-GP model fit gives consistent results with the fit including a GP.

The complete set of model parameters is listed in Table 3. Of note, we sampled eccentricity in as a unit disk, which minimizes geometric biases in sampling and also included a physical prior based on Kipping (2013a). `exoplanet` uses a gradient-based MCMC algorithm that is a generalization of the No U-Turn Sampling method (Hoffman & Gelman 2014; Betancourt 2016) implemented in pymc3 (Salvatier et al. 2016; Theano Development Team 2016). We ran the sampler for 8000 tuning samples and then drew 2000 samples in each of 4 independent chains for a total of 8000 samples. The model showed strong agreement between the four chains, indicating excellent convergence. The complete set of modeled outputs is found in Table 4.

5. Discussion

Determining the atmospheric composition of a sub-Neptune such as TOI-1437 b would provide insight into some of the many processes of these planets that are not well understood, such as their formation and interior composition. Shown in Figure 7 is a mass–radius diagram, where known planets are represented as gray circles, and TOI-1437 b is indicated by the large black circle. Due to their wide range of equilibrium temperatures (most falling between 400 and 1200 K; Crossfield & Kreidberg 2017), sub-Neptunes are thought to have a large range of atmospheric compositions (Kite et al. 2020). Although larger (2.5–4.0 $R_\oplus$) sub-Neptunes are expected to retain most of their primordial H/He envelopes, intermediate worlds (1.5–2.5 $R_\oplus$), such as TOI-1437 b, are expected to be extremely diverse in atmospheric composition. Planets with $R_p > 2.0\,R_\oplus$ could be water-ocean worlds that contain dense steam

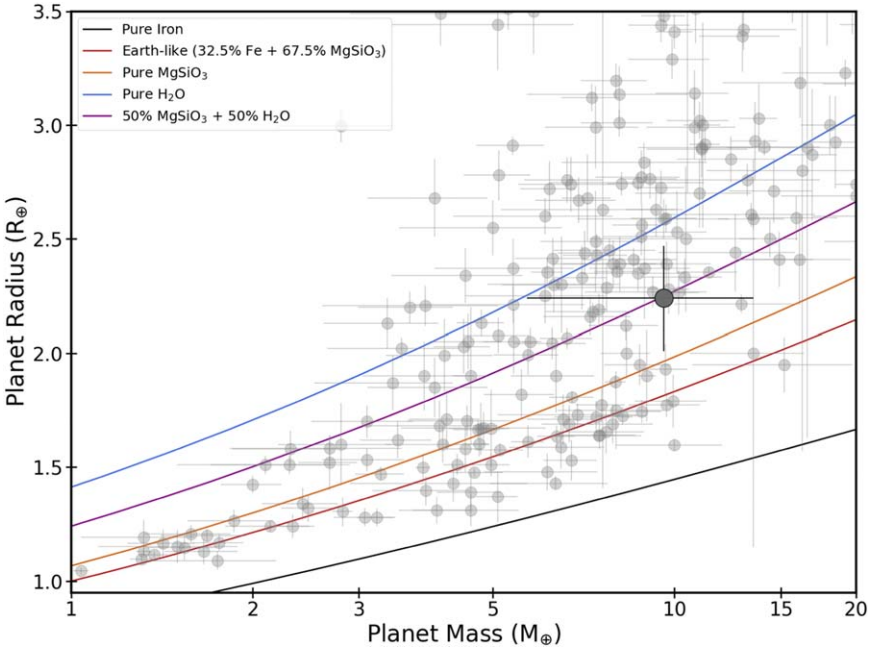

Figure 7. Representation of TOI-1437 b as it falls on a mass–radius diagram (large black circle). Individual solid lines are theoretical mass–radius curves for planets whose composition is specified in the figure legend. Light gray circles indicate the population of planets between 1.0 and 3.5 $R_{\oplus}$ that have measured masses.

Table 4
Modeling Results

Parameter	Median	$+1\sigma$	-1σ
Stellar Radius ($R_{\odot}$)	1.17	0.11	0.12
Stellar Density ($\rho_{\odot}$)	0.91	0.23	0.18
Orbital Period (days)	18.840942	0.000060	0.000068
Transit Epoch (BJD)	2459360.1652	0.0012	0.0012
Impact Parameter	0.24	0.24	0.17
Planet-to-star Radius Ratio	0.01746	0.00047	0.00039
Limb Darkening u_1	0.19	0.21	0.14
Limb Darkening u_2	0.57	0.22	0.30
Orbital Eccentricity	0.17	0.11	0.09
Periastron Angle (rad)	−1.68	0.57	0.45
Radial Velocity Semiamplitude ($m\ s^{-1}$)	2.24	0.68	0.71
TESS Jitter (ppt)	0.4222	0.0024	0.0024
TESS GP ρ (days)	1.02	0.22	0.17
TESS GP σ (ppt)	0.0747	0.0058	0.005
HIRES Jitter ($m\ s^{-1}$)	0.41	0.61	0.21
APF Jitter ($m\ s^{-1}$)	4.3	1.2	1.4
RV GP ρ (days)	6.1	3.0	2.0
RV GP σ ($m\ s^{-1}$)	4.18	0.43	0.38
Planetary Radius ($R_{\oplus}$)	2.24	0.23	0.22
Planetary Mass ($M_{\oplus}$)	9.6	3.9	3.3
Semimajor Axis to Stellar Radius Ratio	25.7	2.0	1.8
Semimajor Axis (au)	0.140	0.018	0.017
Orbital Inclination(deg)	89.53	0.33	0.46
Transit Duration (hr)	4.65	0.45	0.50
Insolation ($S_{\oplus}$)	82.0	14.0	12.0

atmospheres (Bean et al. 2021) or worlds hosting deep magma oceans (Kite et al. 2020) resulting in H_2- or H_2O-rich envelopes that are shrouded with silicate species (Schlichting & Young 2022). Based on its location within Figure 7, TOI-1437 b falls directly on the composition line of 50% $MgSiO_3$ + 50% H_2O. Although further observations would be necessary to determine this, TOI-1437 b is likely a volatile-rich planet that lacks an extended hydrogen atmosphere, but could be dominated by other gases such as CO_2.

Additionally, our measurements are consistent with a single planet model for the system. Continued monitoring of the system with more precise measurements may uncover additional planets in the system, including transit-timing-variation evidence. Follow-up observations could be conducted with the James Webb Space Telescope (JWST) if the system is considered to be a favorable target. To determine whether TOI-1437 b is a strong candidate for atmospheric characterization with JWST, we utilize the transmission spectroscopy metric (TSM) defined by Kempton et al. (2018). The TSM is proportional to the expected transmission spectroscopy signal-to-noise, based on the strength of spectral features, brightness of the host star, and mass and radius of the planet. The TSM value calculated for TOI-1437 b is determined to be 17. As Kempton et al. (2018) recommends that planets with TSM > 90 for $1.5 < R_p < 10\ R_{\oplus}$ be selected as high-quality atmospheric characterization targets among TESS planetary candidates, TOI-1437 b can be considered as a medium priority target for follow-up observations with JWST.

Although TESS observations have led to the discovery of planets orbiting solar analogs (Eberhardt et al. 2023), the majority of TESS discoveries have occurred for stars with masses less than solar. TOI-1437 is not a true solar analog, since it is ∼10% more massive and ∼17% larger than the Sun, placing it even further into the tail of the typical TESS exoplanet host distribution. Even so, studying the parameters such as stellar mass, age, and composition of TOI-1437 could enable an improved understanding of how planetary system evolution is affected by these variations in comparison to the characteristics of the Sun (Gaidos 1998). TOI-1437 could thus provide a benchmark for systems that fall close to solar analogs, where the formation, evolution, and architecture of planetary systems around such stars remains difficult to constrain.

6. Conclusions

Continued discoveries from TESS are providing increasing insight into the sub-Neptune population of exoplanets, their potential properties, and evolution through time. This work identifies TOI-1437 as a planetary system consisting of a sub-Neptune orbiting a near-solar analog, which is a class of host star that is relatively underrepresented within the stellar demographic known to host sub-Neptunes. Combining our transit model alongside RV analysis with APF/Levy and Keck/HIRES allowed us to measure the planetary radius and system stellar properties, and to constrain the mass of the planet within 3σ. TOI-1437 observations with high-resolution near-infrared AO and optical imaging combined with Gaia analysis indicate no evidence for additional stellar companions within the system, allowing us to be confident that our signals are representative of planet TOI-1437 b. Although no other planets have yet been detected within the system, continuation of RV monitoring may reveal planetary companions that improve our understanding of demographics and orbital dynamics in sub-Neptune systems.

Acknowledgments

We thank the time assignment committees of the University of California, the California Institute of Technology, NASA, and the University of Hawaii for supporting the TESS-Keck Survey with observing time at Keck Observatory and on the Automated Planet Finder. We thank NASA for funding associated with our Key Strategic Mission Support project. We gratefully acknowledge the efforts and dedication of the Keck Observatory staff for support of HIRES and remote observing. We recognize and acknowledge the cultural role and reverence that the summit of Maunakea has within the indigenous Hawaiian community. We are deeply grateful to have the opportunity to conduct observations from this mountain. We thank Ken and Gloria Levy, who supported the construction of the Levy Spectrometer on the Automated Planet Finder. We thank the University of California and Google for supporting Lick Observatory and the UCO staff for their dedicated work scheduling and operating the telescopes of Lick Observatory. This paper is based on data collected by the TESS mission. Funding for the TESS mission is provided by the NASA Explorer Program. This paper includes data collected by the TESS mission that are publicly available from the Mikulski Archive for Space Telescopes (MAST). Data was taken from the TESS Input Catalog (STScI 2018).

D.P. acknowledges support from the NASA FINESST Fellowship issued via grant No. 80NSSC22K1319.

M.L.H. would like to acknowledge NASA support via the FINESST Planetary Science Division, NASA award number 80NSSC21K1536.

D.R.C. acknowledges partial support from NASA grant 18-2XRP18_2-0007.

D.H. acknowledges support from the Alfred P. Sloan Foundation, the National Aeronautics and Space Administration (80NSSC21K0652) and the Australian Research Council (FT200100871).

J.L.-B. was partly funded by the Ramón y Cajal program with code RYC2021-031640-I. and by the Spanish MCIN/AEI/10.13039/501100011033 grant PID2019-107061GB-C61.

J.M.A.M. is supported by the National Science Foundation Graduate Research Fellowship Program under grant No. DGE-1842400.

This research has made use of the Exoplanet Follow-up Observation Program (ExoFOP; DOI: 10.26134/ExoFOP5) website, which is operated by the California Institute of Technology, under contract with the National Aeronautics and Space Administration under the Exoplanet Exploration Program.

Some of the observations in this paper made use of the High-Resolution Imaging instrument 'Alopeke and were obtained under Gemini LLP Proposal Number: GN/S-2021A-LP-105. 'Alopeke was funded by the NASA Exoplanet Exploration Program and built at the NASA Ames Research Center by Steve B. Howell, Nic Scott, Elliott P. Horch, and Emmett Quigley. Alopeke was mounted on the Gemini North telescope of the international Gemini Observatory, a program of NSF's OIR Lab, which is managed by the Association of Universities for Research in Astronomy (AURA) under a cooperative agreement with the National Science Foundation on behalf of the Gemini partnership: the National Science Foundation (United States), National Research Council (Canada), Agencia Nacional de Investigación y Desarrollo (Chile), Ministerio de Ciencia, Tecnología e Innovación (Argentina), Ministério da Ciência, Tecnologia, Inovações e Comunicações (Brazil), and Korea Astronomy and Space Science Institute (Republic of Korea).

This research was carried out in part at the Jet Propulsion Laboratory, California Institute of Technology, under a contract with the National Aeronautics and Space Administration (80NM0018D0004).

The authors thank Eric Mamajek for helpful discussions that improved the quality of this manuscript.

ORCID iDs

Daria Pidhorodetska https://orcid.org/0000-0001-9771-7953
Emily A. Gilbert https://orcid.org/0000-0002-0388-8004
Stephen R. Kane https://orcid.org/0000-0002-7084-0529
Thomas Barclay https://orcid.org/0000-0001-7139-2724
Alex S. Polanski https://orcid.org/0000-0001-7047-8681
Michelle L. Hill https://orcid.org/0000-0002-0139-4756
Keivan G. Stassun https://orcid.org/0000-0002-3481-9052
Steven Giacalone https://orcid.org/0000-0002-8965-3969
David R. Ciardi https://orcid.org/0000-0002-5741-3047
Andrew W. Boyle https://orcid.org/0000-0001-6037-2971
Steve B. Howell https://orcid.org/0000-0002-2532-2853
Jorge Lillo-Box https://orcid.org/0000-0003-3742-1987
Mason G. MacDougall https://orcid.org/0000-0003-2562-9043
Tara Fetherolf https://orcid.org/0000-0002-3551-279X
Natalie M. Batalha https://orcid.org/0000-0002-7030-9519
Courtney Dressing https://orcid.org/0000-0001-8189-0233
Benjamin Fulton https://orcid.org/0000-0003-3504-5316
Andrew W. Howard https://orcid.org/0000-0001-8638-0320
Daniel Huber https://orcid.org/0000-0001-8832-4488
Howard Isaacson https://orcid.org/0000-0002-0531-1073
Erik A. Petigura https://orcid.org/0000-0003-0967-2893
Paul Robertson https://orcid.org/0000-0003-0149-9678
Lauren M. Weiss https://orcid.org/0000-0002-3725-3058
Isabel Angelo https://orcid.org/0000-0002-9751-2664
Corey Beard https://orcid.org/0000-0001-7708-2364
Aida Behmard https://orcid.org/0000-0003-0012-9093
Sarah Blunt https://orcid.org/0000-0002-3199-2888
Casey L. Brinkman https://orcid.org/0000-0002-4480-310X
Ashley Chontos https://orcid.org/0000-0003-1125-2564
Fei Dai https://orcid.org/0000-0002-8958-0683
Paul A. Dalba https://orcid.org/0000-0002-4297-5506
Rae Holcomb https://orcid.org/0000-0002-5034-9476

Jack Lubin https://orcid.org/0000-0001-8342-7736
Andrew W. Mayo https://orcid.org/0000-0002-7216-2135
Joseph M. Akana Murphy https://orcid.org/0000-0001-8898-8284
Malena Rice https://orcid.org/0000-0002-7670-670X
Ryan Rubenzahl https://orcid.org/0000-0003-3856-3143
Nicholas Scarsdale https://orcid.org/0000-0003-3623-7280
Emma V. Turtelboom https://orcid.org/0000-0002-1845-2617
Dakotah Tyler https://orcid.org/0000-0003-0298-4667
Judah Van Zandt https://orcid.org/0000-0002-4290-6826
Edward W. Schwieterman https://orcid.org/0000-0002-2949-2163

References

Aller, A., Lillo-Box, J., Jones, D., Miranda, L. F., & Barceló Forteza, S. 2020, A&A, 635, A128
Bean, J. L., Raymond, S. N., & Owen, J. E. 2021, JGRE, 126, e06639
Betancourt, M. 2016, arXiv:1604.00695
Bhatti, W., Bouma, L., Joshua, J., & Price-Whelan, A. 2020, waqasbhatti/astrobase: astrobase v0.5.0, Zenodo, doi:10.5281/zenodo.3723832
Bluhm, P., Pallé, E., Molaverdikhani, K., et al. 2021, A&A, 650, A78
Borucki, W. J., Koch, D., Basri, G., et al. 2010, Sci, 327, 977
Burke, C. J., Christiansen, J. L., Mullally, F., et al. 2015, ApJ, 809, 8
Chabrier, G. 2001, ApJ, 554, 1274
Chontos, A., Murphy, J. M. A., MacDougall, M. G., et al. 2022, AJ, 163, 297
Ciardi, D. R., Beichman, C. A., Horch, E. P., & Howell, S. B. 2015, ApJ, 805, 16
Crossfield, I. J. M., & Kreidberg, L. 2017, AJ, 154, 261
Dekany, R., Roberts, J., Burruss, R., et al. 2013, ApJ, 776, 130
Dressing, C. D., & Charbonneau, D. 2013, ApJ, 767, 95
Eberhardt, J., Hobson, M. J., Henning, T., et al. 2023, AJ, 166, 271
Foreman-Mackey, D. 2018, RNAAS, 2, 31
Foreman-Mackey, D., Luger, R., Agol, E., et al. 2021, Exoplanet: Gradient-based Probabilistic Inference for Exoplanet Data & other Astronomical Time Series, v0.5.1, Zenodo, doi:10.5281/zenodo.1998447
Foreman-Mackey, D., Agol, E., Ambikasaran, S., & Angus, R. 2017, AJ, 154, 220
Fortney, J. J., Mordasini, C., Nettelmann, N., et al. 2013, ApJ, 775, 80
Fressin, F., Torres, G., Charbonneau, D., et al. 2013, ApJ, 766, 81
Fulton, B. J., Petigura, E. A., Blunt, S., & Sinukoff, E. 2018, PASP, 130, 044504
Fulton, B. J., Petigura, E. A., Howard, A. W., et al. 2017, AJ, 154, 109
Furlan, E., & Howell, S. B. 2020, ApJ, 898, 47
Furlan, E., Ciardi, D. R., Everett, M. E., et al. 2017, AJ, 153, 71
Gaia Collaboration, Vallenari, A., Brown, A. G. A., et al. 2023, A&A, 674, A1
Gaidos, E. J. 1998, PASP, 110, 1259
Gavel, D., Kupke, R., Dillon, D., et al. 2014, Proc. SPIE, 9148, 914805
Girardi, L., Barbieri, M., Groenewegen, M. A. T., et al. 2012, ASSP, 26, 165
Guerrero, N. M., Seager, S., Huang, C. X., et al. 2021, ApJS, 254, 39
Guzmán-Mesa, A., Kitzmann, D., Mordasini, C., & Heng, K. 2022, MNRAS, 513, 4015
Hayward, T. L., Brandl, B., Pirger, B., et al. 2001, PASP, 113, 105
Hoffman, M. D., & Gelman, A. 2014, JMLR, 15, 1593, https://jmlr.org/papers/volume15/hoffman14a/hoffman14a.pdf
Hormuth, F., Brandner, W., Hippler, S., & Henning, T. 2008, JPhCS, 131, 012051
Howard, A. W., Johnson, J. A., Marcy, G. W., et al. 2010, ApJ, 721, 1467
Howe, A. R., Burrows, A., & Verne, W. 2014, ApJ, 787, 173
Howell, S. B., & Furlan, E. 2022, FrASS, 9, 871163
Howell, S. B., Sobeck, C., Haas, M., et al. 2014, PASP, 126, 398
Howell, S. B., Scott, N. J., Matson, R. A., et al. 2021, FrASS, 8, 10
Howell, S. B., Everett, M. E., Sherry, W., Horch, E., & Ciardi, D. R. 2011, AJ, 142, 19
Hsu, D. C., Ford, E. B., Ragozzine, D., & Ashby, K. 2019, AJ, 158, 109
Husser, T. O., Wende-von Berg, S., Dreizler, S., et al. 2013, A&A, 553, A6
Isaacson, H., & Fischer, D. 2010, ApJ, 725, 875
Jenkins, J. M., Twicken, J. D., McCauliff, S., et al. 2016, Proc. SPIE, 9913, 99133E
Kane, S. R., Arney, G. N., Byrne, P. K., et al. 2021a, JGRE, 126, e06643
Kane, S. R., Bean, J. L., Campante, T. L., et al. 2021b, PASP, 133, 014402
Kempton, E. M.-R., Bean, J. L., Louie, D. R., et al. 2018, PASP, 130, 114401
Kipping, D. M. 2013a, MNRAS, 435, 2152
Kipping, D. M. 2013b, MNRAS, 434, L51
Kite, E. S., Fegley, B., Jr., Schaefer, L., & Ford, E. B. 2020, ApJ, 891, 111
Kupke, R., Gavel, D., Roskosi, C., et al. 2012, Proc. SPIE, 8447, 84473G
Lange, S., Akana Murphy, J. M., Batalha, N. M., et al. 2024, AJ, 167, 282
Léger, A., Rouan, D., Schneider, J., et al. 2009, A&A, 506, 287
Lester, K. V., Matson, R. A., Howell, S. B., et al. 2021, AJ, 162, 75
Lillo-Box, J., Barrado, D., & Bouy, H. 2012, A&A, 546, A10
Lillo-Box, J., Barrado, D., & Bouy, H. 2014, A&A, 566, A103
Lopez, E. D., & Fortney, J. J. 2014, ApJ, 792, 1
Lubin, J., Van Zandt, J., Holcomb, R., et al. 2022, AJ, 163, 101
Lund, M. B., & Ciardi, D. 2020, BAA, 52, 1
Matson, R. A., Howell, S. B., Horch, E. P., & Everett, M. E. 2018, AJ, 156, 31
McGurk, R., Rockosi, C., Gavel, D., et al. 2014, Proc. SPIE, 9148, 91483A
Misener, W., Schlichting, H. E., & Young, E. D. 2023, MNRAS, 524, 981
Morley, C. V., Kreidberg, L., Rustamkulov, Z., Robinson, T., & Fortney, J. J. 2017, ApJ, 850, 121
Moses, J. I., Line, M. R., Visscher, C., et al. 2013, ApJ, 777, 34
Mugrauer, M., & Michel, K.-U. 2020, AN, 341, 996
Mugrauer, M., & Michel, K.-U. 2021, AN, 342, 840
Mugrauer, M., Zander, J., & Michel, K.-U. 2022, AN, 343, e24017
Petigura, E. A., Howard, A. W., & Marcy, G. W. 2013, PNAS, 110, 19273
Raymond, S. N., Boulet, T., Izidoro, A., Esteves, L., & Bitsch, B. 2018, MNRAS, 479, L81
Ricker, G. R., Winn, J. N., Vanderspek, R., et al. 2015, JATIS, 1, 014003
Rogers, L. A. 2015, ApJ, 801, 41
Rogers, L. A., Bodenheimer, P., Lissauer, J. J., & Seager, S. 2011, ApJ, 738, 59
Salvatier, J., Wiecki, T. V., & Fonnesbeck, C. 2016, PeerJ Computer Science, 2, e55
Savel, A. B., Dressing, C. D., Hirsch, L. A., et al. 2020, AJ, 160, 287
Savel, A. B., Hirsch, L. A., Gill, H., Dressing, C. D., & Ciardi, D. R. 2022, PASP, 134, 124501
Scarsdale, N., Murphy, J. M. A., Batalha, N. M., et al. 2021, AJ, 162, 215
Schlegel, D. J., Finkbeiner, D. P., & Davis, M. 1998, ApJ, 500, 525
Schlichting, H. E. 2014, ApJL, 795, L15
Schlichting, H. E., & Young, E. D. 2022, PSJ, 3, 127
Scott, N. J., Howell, S. B., Gnilka, C. L., et al. 2021, FrASS, 8, 138
Soto, M. G., Anglada-Escudé, G., Dreizler, S., et al. 2021, A&A, 649, A144
Stassun, K. G., Collins, K. A., & Gaudi, B. S. 2017, AJ, 153, 136
Stassun, K. G., Corsaro, E., Pepper, J. A., & Gaudi, B. S. 2018, AJ, 155, 22
Stassun, K. G., & Torres, G. 2016, AJ, 152, 180
Stassun, K. G., & Torres, G. 2021, ApJL, 907, L33
STScI 2018, TESS Input Catalog and Candidate Target List, STScI/MAST, doi:10.17909/FWDT-2X66
Strehl, K. 1902, AN, 158, 89
Theano Development Team 2016, arXiv:1605.02688
Torres, G., Andersen, J., & Giménez, A. 2010, A&ARv, 18, 67
Unterborn, C. T., Desch, S. J., Haldemann, J., et al. 2023, ApJ, 944, 42
Vogt, S. S., Allen, S. L., Bigelow, B. C., et al. 1994, Proc. SPIE, 2198, 362
Vogt, S. S., Radovan, M., Kibrick, R., et al. 2014, PASP, 126, 359
Wolfgang, A., Rogers, L. A., & Ford, E. B. 2016, ApJ, 825, 19
Ziegler, C., Tokovinin, A., Briceño, C., et al. 2020, AJ, 159, 19